Multiple scattering by a collection of randomly located obstacles Part IV: The effect of the pair correlation function

Kristensson, Gerhard; Gustavsson, Magnus; Wellander, Niklas

2021

Document Version:
Publisher's PDF, also known as Version of record

CODEN:LUTEDX/(TEAT-7272)/1-23/(2021)

Multiple scattering by a collection of randomly located obstacles
Part IV: The effect of the pair correlation function

Gerhard Kristensson, Magnus Gustavsson,
and Niklas Wellander

Electromagnetic Theory
Department of Electrical and Information Technology
Lund University
Sweden

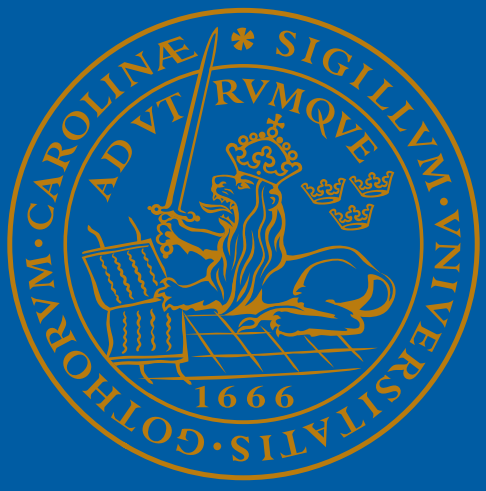

(TEAT-7272)/1-23/(2021): G. Kristensson *et al.*, Multiple scattering by a collection of randomly ..., Part IV ...

Gerhard Kristensson
Gerhard.Kristensson@eit.lth.se

Department of Electrical and Information Technology
Electromagnetics and Nanoelectronics
Lund University
P.O. Box 118
SE-221 00 Lund
Sweden

Magnus Gustavsson
Magnus.Gustafsson@foi.se

Swedish Defence Research Agency, FOI
P.O. Box 1165
SE-581 11 Linköping
Sweden

Niklas Wellander
Niklas.Wellander@foi.se

Swedish Defence Research Agency, FOI
P.O. Box 1165
SE-581 11 Linköping
Sweden

and

Department of Electrical and Information Technology
Electromagnetics and Nanoelectronics
Lund University
P.O. Box 118
SE-221 00 Lund
Sweden

Editor: Mats Gustafsson

Abstract

The effect of two different pair correlation functions, used to model multiple scattering in a slab filled with randomly located spherical particles, is investigated. Specifically, the Percus-Yevick approximation is employed and a comparison with the simple hole correction is made. The kernel entries of the hole correction have an analytic solution, which makes the numerical solution of the integral equations possible. The kernel entries of Percus-Yevick approximation are integrated numerically after a subtraction of the slowly converging part in the integrand. Several numerical examples illustrate the effect of the two pair correlation functions, and we also make a comparison with the predictions Bouguer-Beer law gives.

1 Introduction

Electromagnetic wave propagation in particulate media serves as an instrument to infer the underlying properties and characteristics of the medium, such as shape, size, and density of the particles, but also parameters as attenuation of the transmitted field. The topic has a long tradition and many successful results have been reported in the past. A review of the field can be found in the references [7, 13, 15, 18, 22, 24].

Here, the approach employed to find the coherent (ensemble averaged) electromagnetic field in a slab is an extension of the integral equation method, which is presented in detail in [15]. This approach applies to a general problem (any confinement, particle shape, or excitation), but, for simplicity, we here restrict ourselves to a plane wave impinging at normal incidence on a slab filled with spherical particles. To further develop the method, we study the effect of different pair correlation functions — the hole correction (HC) and the Percus-Yevick (P-Y) approximation — on transmission and reflection. This problem has been studied earlier [3, 4, 23], and also compared to experimental data [27], but with the use of another method — the homogenization method, which for higher frequencies is less accurate. The Percus-Yevick approximation alters the particle distribution in the vicinity of a particle. The particles at the boundary of the slab also show a modified distribution (they have only particles on one side), but how this modification should be modeled is not well understood, and this contribution is not modeled in this paper.

The traditional method to find the coherent (ensemble averaged) field in a slab or half space is by assigning a wavenumber to the medium found by fitting a trial exponential function to a set of integral identities, see *e.g.*, [24]. This is essentially a homogenization method, and it is successful if the frequency is low, but at higher frequencies or larger particle size, several wavenumbers play an equal role and no single material parameter can be assigned to the slab [8–10]. When the homogenization method applies, the material artificially looks like a homogeneous material, and it can be characterized by a bulk permittivity ϵ_{eff} and permeability μ_{eff}. The integral equation method employed in this paper avoids this identification with a homogenized medium. A comparison of the present method and the traditional homogenization has been reported earlier, see *e.g.*, [12].

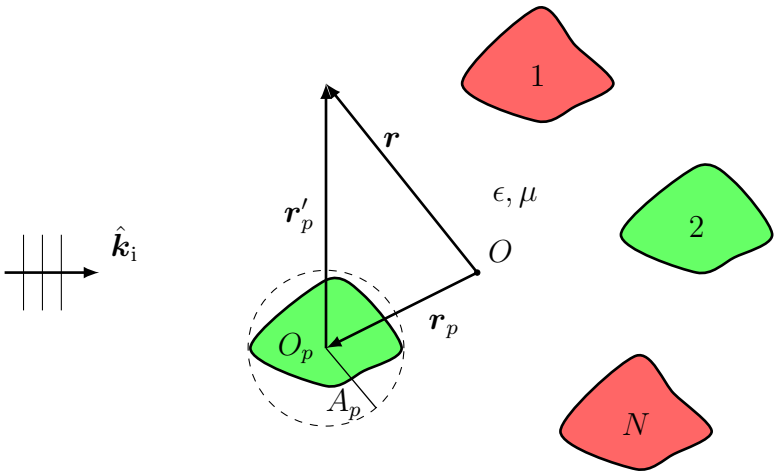

Figure 1: The geometry of the collection of N particles. The positions of the local origins are $\boldsymbol{r}_p$, $p = 1, \ldots, N$, and the radius of the minimum circumscribed sphere of each individual particle is A_p. A plane wave impinges on the configuration from the left in the direction $\hat{\boldsymbol{k}}_\mathrm{i}$.

This paper starts with a short overview of the deterministic multiple scattering problem in Section 2. In Section 3, the solution of the coherent field is stated, and the reflection and transmitted fields are stated in Section 4. The main numerical results of this paper are presented in Section 5, which are also discussed in the concluding Section 6. The paper ends by a series of appendices, where the notation used in the paper is explained, and where some detailed calculations are presented.

2 Multiple scattering — deterministic problem

The geometry of the deterministic problem is depicted in Figure 1. There are N different or equal particles located in a lossless, homogeneous background with permittivity ϵ and permeability μ. The wavenumber of the background material is denoted k. The local origin, O_p, of particle p is positioned at $\boldsymbol{r}_p$, $p = 1, 2, \ldots, N$, with respect to the common origin O.

The deterministic multiple scattering problem can be formulated and solved by the employment of the integral representation of the electric field [17]. The other important tool in the solution of the problem is the decomposition of the Green dyadic for the electric field in free space in regular and radiating spherical vector waves, $\boldsymbol{v}_n(k\boldsymbol{r})$ and $\boldsymbol{u}_n(k\boldsymbol{r})$, respectively (see Appendix A for details and definitions of the spherical vector waves). The details of the solution are presented in [15, 17], and here we only give the final result. The most relevant incident electric field in this paper is a plane wave of arbitrary strength and polarization $\boldsymbol{E}_0$.

$$\boldsymbol{E}_\mathrm{i}(\boldsymbol{r}) = \boldsymbol{E}_0 \mathrm{e}^{\mathrm{i}k\hat{\boldsymbol{k}}_\mathrm{i}\cdot\boldsymbol{r}} = \sum_n a_n \boldsymbol{v}_n(k\boldsymbol{r})$$

where the expansion coefficients, a_n, are given by [17]

$$a_n = 4\pi \boldsymbol{a}_n^*(\hat{\boldsymbol{k}}_\mathrm{i}) \cdot \boldsymbol{E}_0 \tag{2.1}$$

The (complex-valued) vector spherical harmonics, $\boldsymbol{a}_n(\hat{\boldsymbol{k}}_\mathrm{i})$, are defined in (A.1), and the summation over the multi-index $n = \{\tau, \sigma, m, l\}$ is over $\tau = 1, 2$, $\sigma = \mathrm{e}, \mathrm{o}$, $m = 0, 1, 2, \ldots, l$, and $l = 1, 2, 3 \ldots$, see also Appendix A and [17] for more details.

The scattered electric field has the form [15]

$$\boldsymbol{E}_\mathrm{s}(\boldsymbol{r}) = \sum_{p=1}^{N} \sum_{n} f_n^p \boldsymbol{u}_n(k(\boldsymbol{r} - \boldsymbol{r}_p)), \quad |\boldsymbol{r} - \boldsymbol{r}_p| > A_p, \ p = 1, 2, \ldots, N \tag{2.2}$$

The coefficients f_n^p depend on the positions, $\boldsymbol{r}_p$, and the properties of all the particles. These coefficients satisfy the linear system of equations ($p = 1, 2, \ldots, N$)

$$f_n^p = \mathrm{e}^{\mathrm{i}k\hat{\boldsymbol{k}}_\mathrm{i}\cdot\boldsymbol{r}_p} \sum_{n'} T_{nn'}^p a_{n'} + \sum_{\substack{q=1 \\ q\neq p}}^{N} \sum_{n'n''} T_{nn'}^p \mathcal{P}_{n'n''}(k(\boldsymbol{r}_q - \boldsymbol{r}_p)) f_{n''}^q \tag{2.3}$$

In this linear system the expansion coefficients of the incident field a_n, the transition matrix $T_{nn'}^p$ of particle p, and the translation matrix $\mathcal{P}_{nn'}(k(\boldsymbol{r}_q - \boldsymbol{r}_p))$ are known. The transition matrix of particle p is defined as the mapping from the expansion coefficients of the exciting field in regular spherical vector waves to the expansion coefficients of the radiating field in outgoing spherical vector waves [17]. The translation matrices of the spherical vector waves, $\mathcal{P}_{nn'}(k\boldsymbol{d})$, are found in Appendix B. Finally, through (2.2), the scattered field is evaluated by the use of the solution f_n^p in (2.3).

3 Randomly distributed particles in a slab

We now confine the positions $\boldsymbol{r}_p$ in (2.3) to a slab $[0, d]$, see Figure 2, and we also let $\boldsymbol{r}_p$ be random variables. Moreover, we assume all particles identical and that the plane wave impinges normally to the slab. This assumption of identical particle simplifies the analysis, and the particles are characterized by a common transition matrix $T_{nn'}$, which does not depend on the position. In the final numerical illustrations, we let the particles be spherical, homogeneous spheres of radius a.

The analysis follows closely [6,15,22,24,26], and we here only give the final result. Assuming the Quasi Crystalline Approximation (QCA) [7], the conditional average $\langle f_n \rangle (z)$ of (2.3), keeping one particle fixed, is [15]

$$\langle f_n \rangle (z) = \mathrm{e}^{\mathrm{i}kz} \sum_{n'} T_{nn'} a_{n'} + k \sum_{n'} \int_a^{d-a} K_{nn'}(z - z') \langle f_{n'} \rangle (z') \, \mathrm{d}z', \ z \in [a, d-a] \tag{3.1}$$

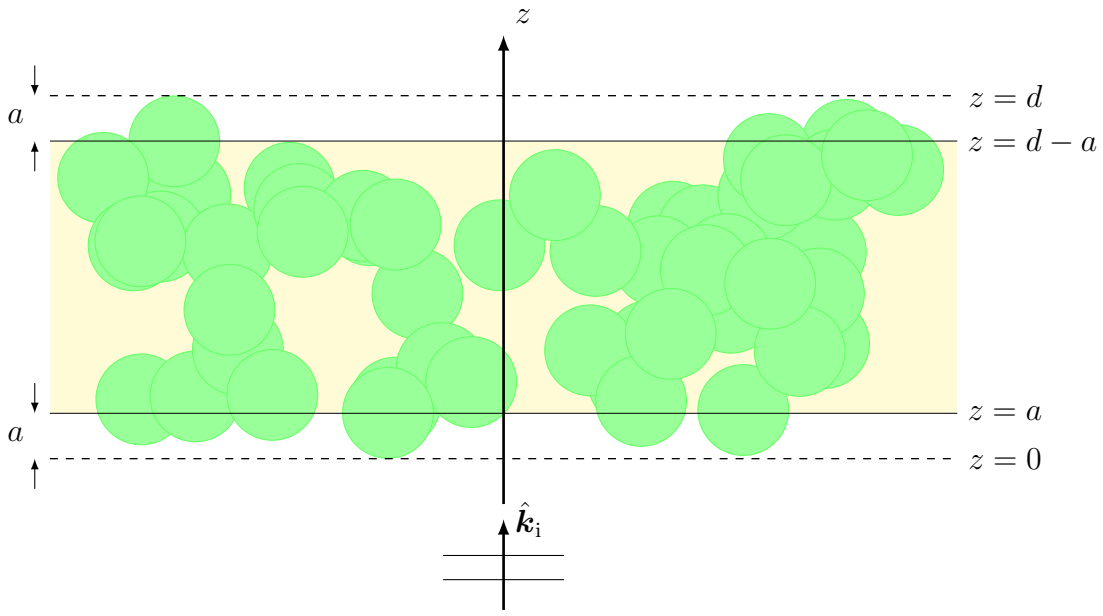

Figure 2: The geometry of the slab. Notice the difference in thickness of the slab $[0, d]$, and the possible locations of the local origins $[a, d-a]$.

where the kernel entries have the form

$$K_{nn'}(z) = \frac{n_0}{k^3} \sum_{n''\lambda} T_{nn''} \mathcal{A}_{n''n'\lambda} I_\lambda(-z) \tag{3.2}$$

The number density of the local origins is denoted n_0. Note that the conditional average is only a function of the depth variable, z, due to the translational invariance of the problem, and that the integration is carried out over the possible locations of the local origins $[a, d-a]$. The set of integral equations is solved with Nyström's method and Gauss-Legendre quadrature points [14]. $\mathcal{A}_{n''n'\lambda}$ are pure real numbers (containing Wigner 3-j symbols), see Appendix B.1. The integrals $I_\lambda(z)$ are presented in the next section.

3.1 Kernel entries

The integrals of the kernel entries in (3.2) have the form [15]

$$I_l(z) = k^2 \int_0^\infty g(r(r_\mathrm{c}, z)) \mathrm{h}_l^{(1)}(kr(r_\mathrm{c}, z)) \mathrm{P}_l(z/r(r_\mathrm{c}, z)) r_\mathrm{c} \, \mathrm{d}r_\mathrm{c} \tag{3.3}$$

where $r(r_\mathrm{c}, z) = \sqrt{r_\mathrm{c}^2 + z^2}$, and $g(r)$ is the pair correlation function [20]. To handle the numerical integration, we divide the pair correlation function $g(r)$ in two parts

$$g(r) = \mathrm{H}(r - 2a) \Big(\underbrace{1}_{\text{HC}} + \underbrace{g(r) - 1}_{\text{P-Y corr}} \Big)$$

where the first term is the hole correction and the second is a correction term subject to the analysis of Percus-Yevick [21].

The kernel entries of the hole correction have an analytic solution [16]. The result is

$$
\begin{aligned}
I_l^{\mathrm{HC}}(z) &= k^2 \int_0^\infty \mathrm{H}(r(r_\mathrm{c},z)-2a)\mathrm{h}_l^{(1)}(kr(r_\mathrm{c},z))\mathrm{P}_l(z/r(r_\mathrm{c},z))r_\mathrm{c}\ \mathrm{d}r_\mathrm{c} \\
&= \begin{cases} \mathrm{i}^l \mathrm{e}^{-\mathrm{i}kz}, & z \le -2a \\ -2ka\mathrm{h}_{l+1}^{(1)}(2ka)\mathrm{P}_l(z/2a) \\ \quad + \sum_{k=0}^{[l/2]} (-1)^k (2l-4k+1)\mathrm{h}_{l-2k}^{(1)}(2ka)\mathrm{P}_{l-2k}(z/2a), & z \in (-2a, 2a) \\ \mathrm{i}^{-l}\mathrm{e}^{\mathrm{i}kz}, & z \ge 2a \end{cases}
\end{aligned}
$$

This analytic result of the integrals $I_l^{\mathrm{HC}}(z)$ is instrumental for the approach presented in this paper. Due to very poor convergence of the infinite integrals, a numerical solution of these integrals is extremely hard. The symbol $[x]$ denotes the integer part of x.

The correction term, containing the Percus-Yevick approximation, can most conveniently be done by numerical integration, provided the convergence rate of the integral is improved. We have

$$
I_l^{\mathrm{Corr}}(z) = k^2 \int_0^\infty \mathrm{H}(r(r_\mathrm{c},z)-2a)\left(g\left(r(r_\mathrm{c},z)\right)-1\right)\mathrm{h}_l^{(1)}(kr(r_\mathrm{c},z))\mathrm{P}_l(z/r(r_\mathrm{c},z))r_\mathrm{c}\ \mathrm{d}r_\mathrm{c} \tag{3.4}
$$

where the pair correlation function is analyzed in detail in Appendix D. The result is

$$
g(r) = 1 + \frac{9fR}{2r}\frac{1+f}{(1-f)^3} + \frac{2R}{r\pi}\int_0^\infty \Bigg(\underbrace{\frac{xF(x)}{1-24fF(x)} - G(x)}_{O(1/x^3)} \Bigg) \sin(rx/R)\ \mathrm{d}x
$$

where the explicit form of the functions $F(x)$ and $G(x)$ are given in (D.1) and (D.2) in Appendix D. Here, the volume fraction is denoted f. Some examples of the pair correlation function $g(r)$ are depicted in Figure 3.

The relation between number density n_0 and volume fraction f for spherical particles with radius a in a slab of thickness d is

$$
f = n_0 \frac{4\pi a^3}{3}\left(1 - \frac{2a}{d}\right)
$$

Note the factor $(1-2a/d)$, which is an effect of different volume references for the number density and the volume fraction (n_0 refers to the volume of possible local origins, while f refers to the confining volume), see Appendix C. For small ratios a/d, this difference in volume reference can be neglected, and the factor can be set to 1.

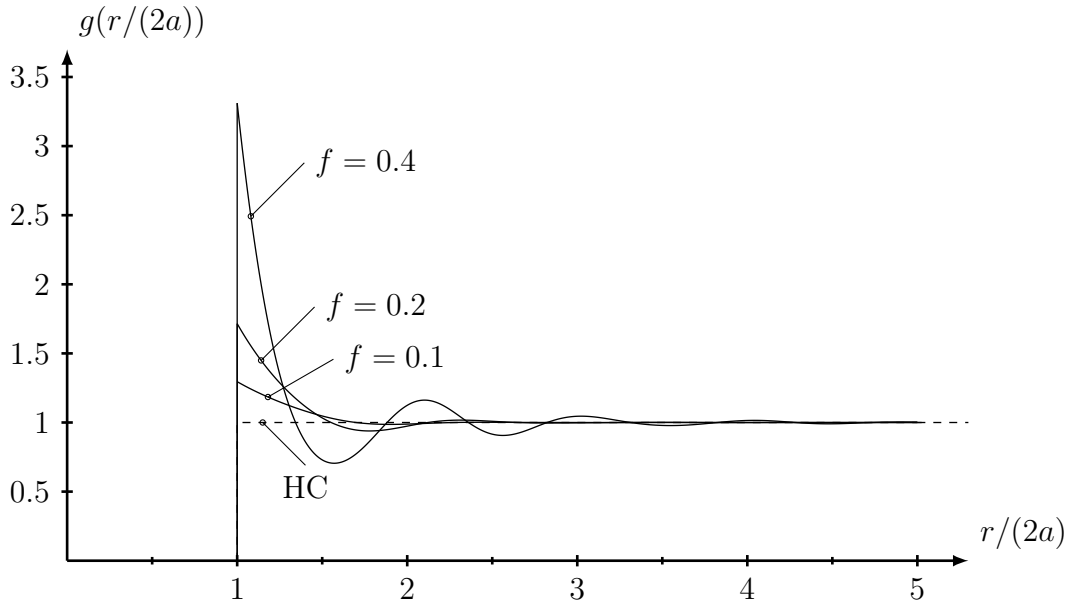

Figure 3: The hole correction (HC) and the Percus-Yevick approximation for volume fraction $f = 0.1$, $f = 0.2$, and $f = 0.4$.

4 Reflection and transmission

With the solution of the integral equations (3.1), we can now compute the coherent (ensemble averaged) transmitted and reflected fields by the particulate slab. The average scattered field of the slab, shown in Figure 2, is obtained by the use of (2.2) and a representation of the radiating spherical vector waves in plane waves [15]. The average transmitted and reflected fields are [15]

$$\langle \boldsymbol{E}_{\mathrm{t}}(z)\rangle = \boldsymbol{E}_0 \mathrm{e}^{\mathrm{i}kz} + \frac{2\pi n_0}{k^2}\mathrm{e}^{\mathrm{i}kz}\sum_n \boldsymbol{a}_n(\hat{\boldsymbol{z}})\int_a^{d-a} \mathrm{e}^{-\mathrm{i}kz'}\,\langle f_n\rangle\,(z')\,\mathrm{d}z', \quad z > d$$

and

$$\langle \boldsymbol{E}_{\mathrm{r}}(z)\rangle = \frac{2\pi n_0}{k^2}\mathrm{e}^{-\mathrm{i}kz}\sum_n \boldsymbol{a}_n(-\hat{\boldsymbol{z}})\int_a^{d-a} \mathrm{e}^{\mathrm{i}kz'}\,\langle f_n\rangle\,(z')\,\mathrm{d}z', \quad z < 0$$

respectively. The complex vector spherical harmonics $\boldsymbol{a}_n(\pm\hat{\boldsymbol{z}})$ are explicitly given in (A.2) and (A.3) in Appendix A. Under the assumption of the QCA, these expressions are the exact solution of the coherent transmitted and reflected fields. These exact expressions can be the starting point to various approximation, such as tenuous approximation and low frequency approximations. These approximations are found in [15].

The transmissivity T and the reflectivity R of the slab are defined as

$$T = \frac{|\langle \boldsymbol{E}_{\mathrm{t}}(d)\rangle|^2}{|\boldsymbol{E}_0|^2} = \left| \boldsymbol{E}_0 + \frac{2\pi n_0}{k^2} \sum_n \boldsymbol{a}_n(\hat{\boldsymbol{z}}) \int_a^{d-a} \mathrm{e}^{-\mathrm{i}kz'} \langle f_n \rangle (z') \, \mathrm{d}z' \right|^2 / |\boldsymbol{E}_0|^2 \tag{4.1}$$

and

$$R = \frac{|\langle \boldsymbol{E}_{\mathrm{r}}(d)\rangle|^2}{|\boldsymbol{E}_0|^2} = \left| \frac{2\pi n_0}{k^2} \sum_n \boldsymbol{a}_n(-\hat{\boldsymbol{z}}) \int_a^{d-a} \mathrm{e}^{\mathrm{i}kz'} \langle f_n \rangle (z') \, \mathrm{d}z' \right|^2 / |\boldsymbol{E}_0|^2 \tag{4.2}$$

respectively.

5 Numerical illustrations

We illustrate the results from above in a series of numerical computations. In all illustrations in this paper, we let the particles be lossless dielectric spheres of radius a, permeability $\epsilon = 1.33^2$, and permeability $\mu = 1$ (non-magnetic material). Three different parameters remain to be varied: the effective electric size ka, the thickness d/a, and the volume fraction f. The effects of varying these three parameters are illustrated in the sections below.

In general, the computations with the Percus-Yevick approximation are much more time-consuming than with the hole correction. This is due to the numerical integration of the integral $I_l^{\mathrm{Corr}}(z)$ in (3.4), which lengthens the computation time considerably. However, all computations shown in this section are conveniently made on a simple personal computer.[1]

5.1 Frequency variation

In Figures 4–5, we illustrate the transmissivity T and the reflectivity R as a function of effective electric size ka for a slab thickness of $d/a = 50$. We show the result with the hole correction (HC) and the Percus-Yevick approximation (P-Y).[2]

In addition to the HC and P-Y curves, we also show transmissivity predicted by the Bouguer-Beer (B-B) law [2, 13, 19]

$$\frac{I_{\mathrm{t,coh}}}{I_0} = \mathrm{e}^{-n_0 \sigma_{\mathrm{ext}}(d-2a)} \tag{5.1}$$

where I_0 is the intensity of the incident wave. Notice that no reflected field is predicted by the Bouguer-Beer law. The thickness of the slab in the Bouguer-Beer law is $d - 2a$, which is an effect of the reduction that has to be made in replacing the particulate media with a homogeneous slab, see [12] for further details on this reduction of slab thickness.

[1] AMD A8-7600 Radeon R7, 10 Compute Cores 4C+6G 3.10 GHz, 16 GB RAM.

[2] The transmission curve for the P-Y approximation is truncated below. The numerical precision (15 digits) is not enough to calculate the exact value at the minimum. Note the strong cancellation that takes place in (4.1) at the minimum.

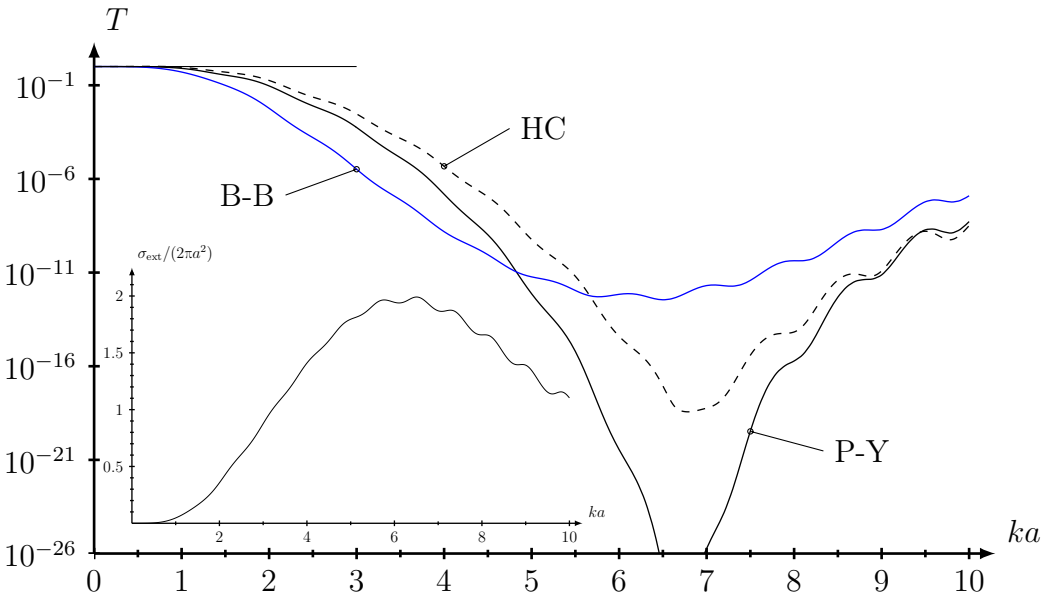

Figure 4: Transmissivity T as a function of ka for the hole correction (HC), the Percus-Yevick (P-Y) approximation, and the Bouguer-Beer (B-B) law. Data of the particles: $\epsilon_r = 1.33^2$ and $\mu_r = 1$. The thickness of the slab is $d = 50a$, and the volume fraction $f = 20\%$. The insert shows the extinction cross section for the individual spherical particles.

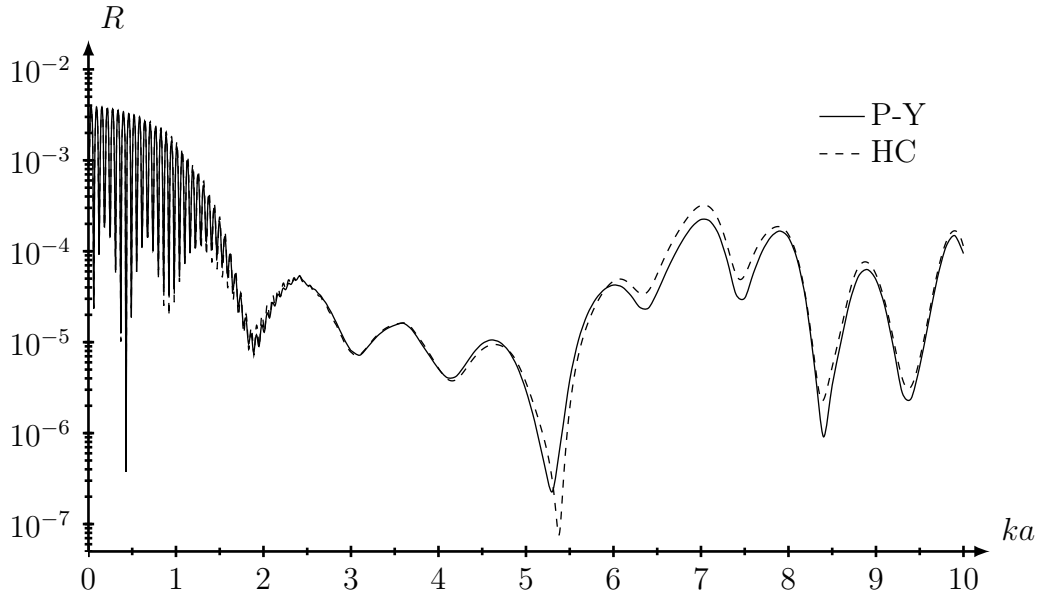

Figure 5: Reflectivity R as a function of ka for the hole correction (HC) and the Percus-Yevick (P-Y) approximation. Data of the particles: $\epsilon_r = 1.33^2$ and $\mu_r = 1$. The thickness of the slab is $d = 50a$, and the volume fraction $f = 20\%$.

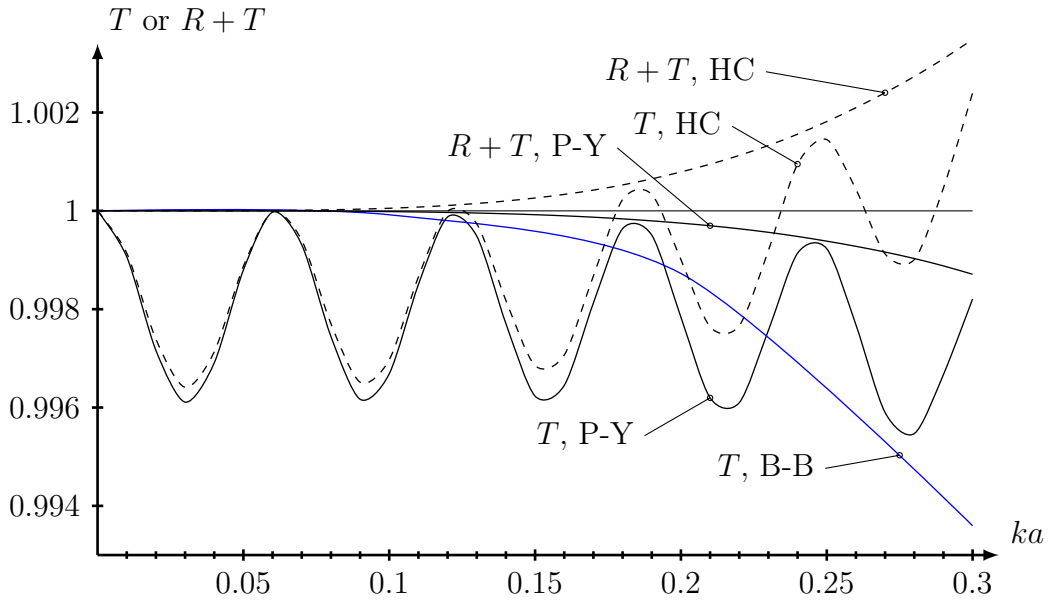

Figure 6: A closeup at low frequencies of the transmissivity T and $R+T$ as a function of ka showing the ripple pattern at low frequencies. The solid lines show the P-Y approximation and the B-B law. The dashed lines show the HC. The line $R+T=1$ is also displayed for clarity. Data of the particles: $\epsilon_{\mathrm{r}}=1.33^2$ and $\mu_{\mathrm{r}}=1$. The thickness of the slab is $d=50a$, and the volume fraction $f=20\%$.

The difference between the HC and the P-Y approximation is larger at transmission than in reflection. This is a general results in all our computations — the pair correlation function affects the reflection field less than the transmission field. The Bouguer-Beer law gives quite inaccurate results for the transmission, which is not surprising, since it is a heuristic model that assumes a linear loss of energy, at transmission, with respect to path length. The Bouguer-Beer law does not consider reflection of coherent energy, which is the reason it is not part of the comparison of the reflectivity results.

Notice the very low transmission values in Figure 4 at frequencies around $ka=6.6$. This is due to the high scattering properties of the individual particles at these frequencies, see the insert in Figure 4. At these frequencies almost all energy is converted into the incoherent contribution, *i.e.*, the wave scattered in other directions at the expense of the energy in the coherent field.

There is another effect present in these computation, which is too small to be visualized in the Figure 4, but clearly seen in reflection in Figure 5. This effect is illustrated in detail in Figure 6. In the closeup, we notice a minute interference effect (note the scale on the ordinate) between waves with energy transport in the positive and negative directions. This ripple in the transmissivity T and the reflectivity R vanishes at higher frequencies due to increasing attenuation of the internally reflected waves, causing the interference effect to gradually disappear. The ripple has a larger amplitude in reflection, since the interaction originates from a field

internally reflected once at the trailing edge. In transmissivity, the interaction is due to a field internally reflected twice at the trailing and leading edges, respectively. Notice that this ripple effect is a consequence of the interference that takes place due to the slab geometry and the monodisperse suspension of spheres, and the effects modify if the conditions change.

In Figure 6, we also show the transmissivity and reflectivity added together, *i.e.*, $R + T$. Notice that there is no ripple in this sum, neither for the HC nor for the P-Y approximation — the ripple effects in the reflectivity and the transmissivity have opposite phase giving a monotonically decreasing curve. Another remarkable effect shown in Figure 6 is that the sum $R + T$ for HC extends above the line 1, which indicates that energy conservation is violated (remember all particles are lossless). We conjecture that this energy violation indicates that the hole correction distribution is not possible to realize for denser media ($f = 20\%$). No such violation of energy conservation is found for the Percus-Yevick approximation. Instead, for the Percus-Yevick approximation, the difference between $R+T$ and 1 gives an indication of the total power contribution of the incoherent or diffuse wave. This fact restricts the use of the hole correction to low volume fractions, and it should not be used with dense media.

5.2 Volume fraction variation

We continue the presentation of numerical results with some transmissivity and reflectivity graphs where the volume fraction f varies, and the frequency, ka, and the thickness, d/a, are fixed.

In Figures 7–8, we illustrate the variation of the transmissivity T and the reflectivity R vs the volume fraction f at two frequencies, $ka = 3, 5$. As expected, the difference between the curves for the two different pair correlation functions vanishes at low volume fractions. This is a consequence of a vanishing difference between the pair correlation functions of the Percus-Yevick approximation and the hole correction. At higher volume fractions, the transmissivity with HC and P-Y approximation starts to deviate. The P-Y approximation gives a higher attenuation, which could be an effect of a higher probability for the particles to be closer to each other compared to the HC. As a consequence, the medium looks denser or the particles look artificially bigger.

The HC and the P-Y approximation distributions also agree well with the transmissivity predicted by the Bouguer-Beer law at low volume fractions. In denser media, the difference between Bouguer-Beer law and the solution of the integral equation becomes larger, and caution has to be taken if the Bouguer-Beer law is used to evaluate the individual extinction cross section of the particles, see (5.1). At the lower frequency, $ka = 3$, the Bouguer-Beer law predicts a smaller transmission than the solution to the integral equation, but at the higher frequency, $ka = 5$, the situation is the opposite (compare Figure 4, $f = 20\%$, $ka = 3$ and $ka = 5$).

No ripple effect is present in these figures, since the frequency ka and the thickness d/a are kept fixed, see Sections 5.1 and 5.3 for a discussion of this ripple effect.

The difference in the result between the two pair correlation functions is again

largest for the transmitted field. There is hardly any difference in the result between the two pair correlation function at reflection, and the difference in transmissivity appears only for denser media.

5.3 Slab thickness variation

The effect of varying the thickness of the slab, $kd = ka\, d/a$, keeping the frequency, ka, and volume fraction, f, fixed, is illustrated in Figures 9–10. The difference between these figures and the results depicted in Figure 4–5 is that in the latter ones the geometry, d/a, is fixed and the effective electric size varies, while in Figures 9–10, the frequency, ka, is fixed and the thickness of the slab, kd, varies, all lengths measured in relation to the wavelength of the incident wave.

At the lower frequency, $ka = 1$, the differences in transmissivity between the hole correction, the Percus-Yevick approximation, and the Bouguer-Beer law are quite large. Again, the ripple effect, due to interaction between forward and backward propagating waves, is larger at reflection than at transmission, for the same reasons as discussed in Section 5.1. The period of the ripple stays the same in these computations since the period is determined by the value of kd and not by the size of the particles. Moreover, the ripple effect gets smaller at higher frequencies, ka, and with increasing thickness, kd, due to larger attenuation of the internal waves at higher frequencies.

6 Conclusions

In this paper, we compare the scattering properties of a particulate slab subject to two different pair correlation functions — the hole correction and the Percus-Yevick approximations. A comparison with the predicted transmission obtained by the use of Bouguer-Beer law is also made. These comparisons are made possible by the solution of a set of integral equations, which gives the exact value of the ensemble averaged fields, provided the Quasi Crystalline Approximation holds. The exact value of the coherent field is suitable for comparisons made in this paper, but also for comparisons with *e.g.*, Monte Carlo simulations, the effect of QCA, and the effective wave number approximation.

The simplest distribution is that of the hole correction, which states that the pair correlation function is unity everywhere in space except inside a ball of radius $2a$. The Percus-Yevick approximation gives a higher probability for the particles to gather close together. Transmission obtained by the Percus-Yevick approximation distribution is in general lower than transmission obtained by the hole correction distribution. With the hole correction distribution, the slab seems to have an apparently lower volume density, which gives somewhat higher transmission. Another interpretation or explanation is that particles do not form clusters with the hole correction distribution, and therefore the particles have an apparently smaller size, and thus higher transmission.

The Percus-Yevick approximation gives a more realistic distribution of the par-

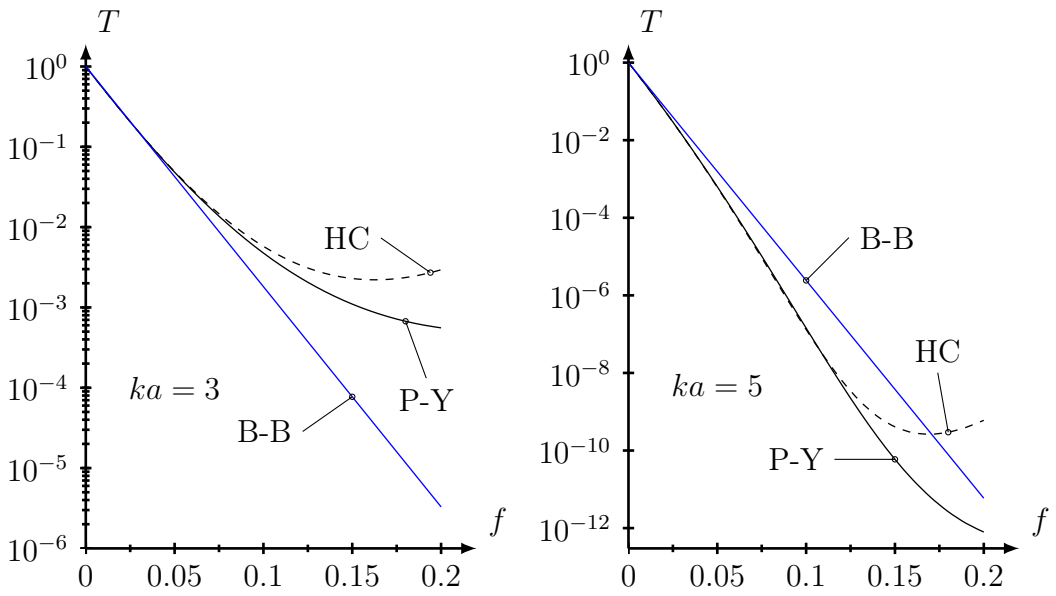

Figure 7: Transmissivity T as a function of the volume fraction f for the hole correction (HC), the Percus-Yevick (P-Y) approximation, and the Bouguer-Beer (B-B) law. Data of the particles: $\epsilon_{\mathrm{r}} = 1.33^2$ and $\mu_{\mathrm{r}} = 1$. The thickness of the slab is $d = 50a$, and $ka = 3$ (left) and $ka = 5$ (right).

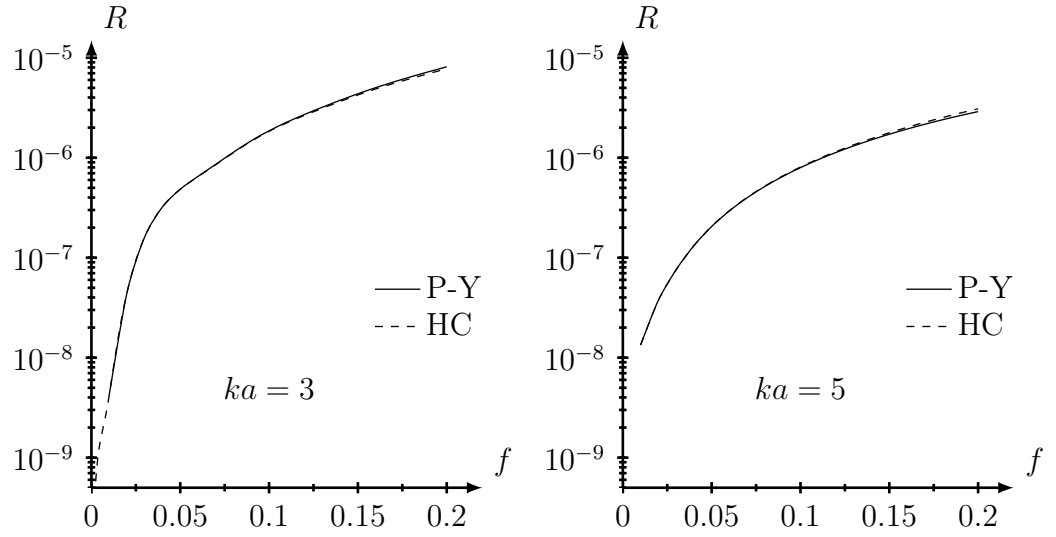

Figure 8: Same as Figure 7, but shows reflectivity R as a function of the volume fraction f for the hole correction (HC) and the Percus-Yevick (P-Y) approximation. As in Figure 7, $ka = 3$ (left) and $ka = 5$ (right).

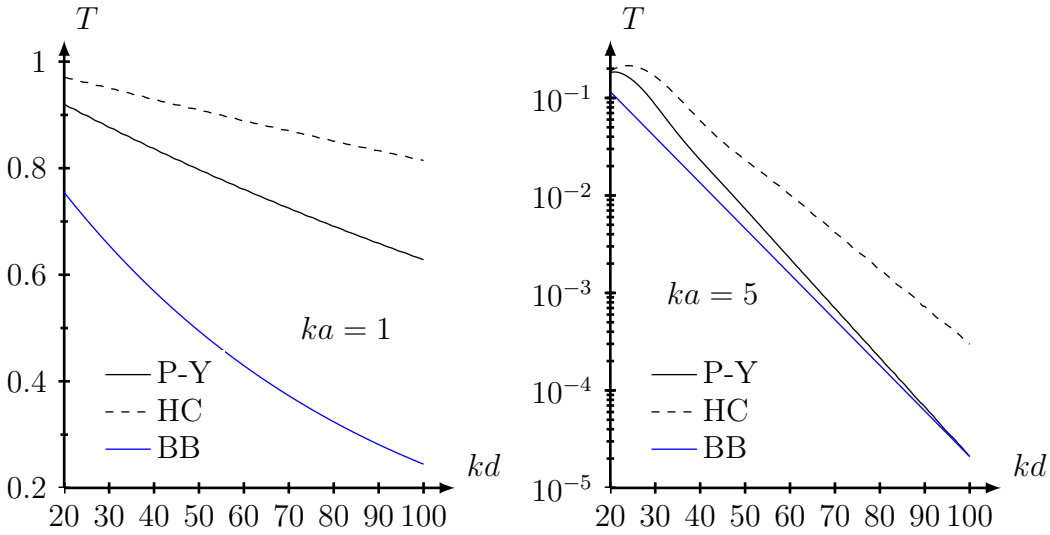

Figure 9: Transmissivity T as a function of the thickness kd for the hole correction (HC), the Percus-Yevick (P-Y) approximation, and the Bouguer-Beer (B-B) law. Data of the particles: $\epsilon_r = 1.33^2$ and $\mu_r = 1$. The frequency is $ka = 1$ (left) and $ka = 5$ (right) and the volume fraction $f = 20\%$. Note the linear scale on the ordinate on the left-hand figure.

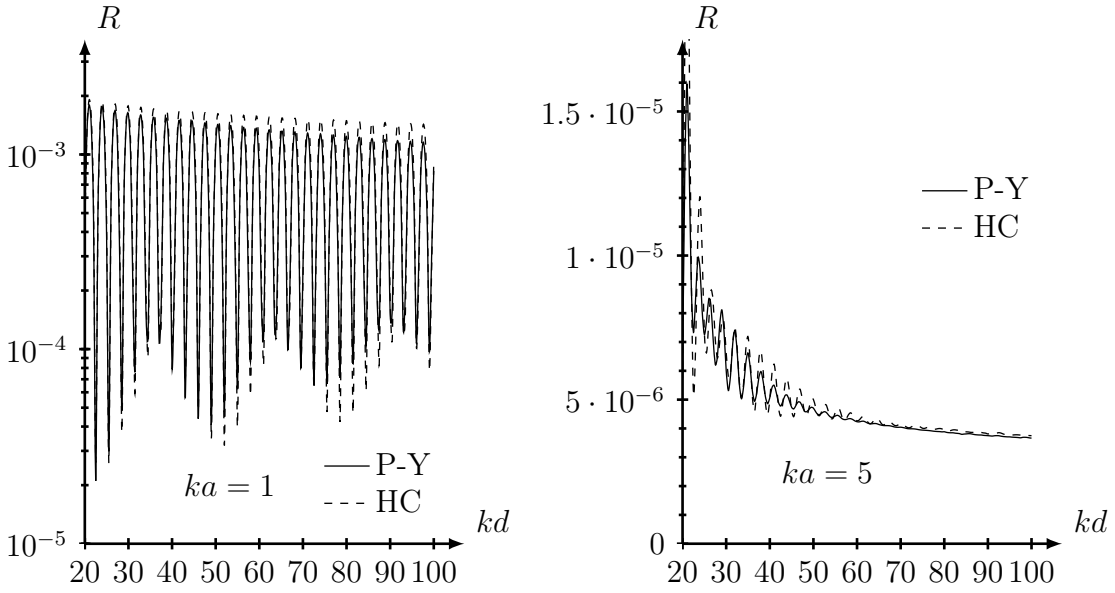

Figure 10: Same as Figure 9, but shows reflectivity R as a function of the thickness kd for the hole correction (HC) and the Percus-Yevick (P-Y) approximation. The frequency is $ka = 1$ (left) and $ka = 5$ (right). Note the linear scale on the ordinate on the right-hand figure.

ticles in the slab. This is corroborated by a study of the energy balance connected to the lossless spherical particles in the slab. The hole correction distribution violates energy conservation at low frequencies and dense media. It is conjectured that the reason for this is that the hole correction distribution generates an unrealizable distribution of particles. No such conflicts seems to appear with the Percus-Yevick approximation. As a consequence, hole correction distribution has a limited use in dense media.

The transmissivity obtained by the Bouguer-Beer law is quite erroneous, due to lack of near field interaction and edge interference effects. The Bouguer-Beer law is often used for extinction cross section measurements, but our calculations show that caution is recommended.

7 Acknowledgement

The research was partially supported by the Swedish Armed Forces R&D programme for Sensors and low observables (FoT SoS, AT.9220421).

Appendix A Functions and transformations

A.1 Vector spherical harmonics and spherical vector waves

The vector spherical harmonic are [17]

$$\begin{cases} \boldsymbol{A}_{1\sigma ml}(\hat{\boldsymbol{r}}) = \dfrac{1}{\sqrt{l(l+1)}}\nabla \times (\boldsymbol{r}\mathrm{Y}_{\sigma ml}(\hat{\boldsymbol{r}})) = \dfrac{1}{\sqrt{l(l+1)}}\nabla \mathrm{Y}_{\sigma ml}(\hat{\boldsymbol{r}}) \times \boldsymbol{r} \\ \boldsymbol{A}_{2\sigma ml}(\hat{\boldsymbol{r}}) = \dfrac{1}{\sqrt{l(l+1)}} r\nabla \mathrm{Y}_{\sigma ml}(\hat{\boldsymbol{r}}) \\ \boldsymbol{A}_{3\sigma ml}(\hat{\boldsymbol{r}}) = \hat{\boldsymbol{r}}\mathrm{Y}_{\sigma ml}(\hat{\boldsymbol{r}}) \end{cases}$$

or explicitly in the spherical unit vectors

$$\begin{cases} \boldsymbol{A}_{1\sigma ml}(\hat{\boldsymbol{r}}) = \dfrac{1}{\sqrt{l(l+1)}} \left(\hat{\boldsymbol{\theta}} \dfrac{1}{\sin\theta} \dfrac{\partial}{\partial \phi} \mathrm{Y}_{\sigma ml}(\hat{\boldsymbol{r}}) - \hat{\boldsymbol{\phi}} \dfrac{\partial}{\partial \theta} \mathrm{Y}_{\sigma ml}(\hat{\boldsymbol{r}}) \right) \\ \boldsymbol{A}_{2\sigma ml}(\hat{\boldsymbol{r}}) = \dfrac{1}{\sqrt{l(l+1)}} \left(\hat{\boldsymbol{\theta}} \dfrac{\partial}{\partial \theta} \mathrm{Y}_{\sigma ml}(\hat{\boldsymbol{r}}) + \hat{\boldsymbol{\phi}} \dfrac{1}{\sin\theta} \dfrac{\partial}{\partial \phi} \mathrm{Y}_{\sigma ml}(\hat{\boldsymbol{r}}) \right) \\ \boldsymbol{A}_{3\sigma ml}(\hat{\boldsymbol{r}}) = \hat{\boldsymbol{r}}\mathrm{Y}_{\sigma ml}(\hat{\boldsymbol{r}}) \end{cases}$$

The spherical harmonics are defined as [17]

$$\mathrm{Y}_{\sigma ml}(\theta,\phi) = \sqrt{\frac{\varepsilon_m}{2\pi}} \sqrt{\frac{2l+1}{2}\frac{(l-m)!}{(l+m)!}} \mathrm{P}_l^m(\cos\theta) \begin{Bmatrix} \cos m\phi \\ \sin m\phi \end{Bmatrix}$$

where the indices σ, m, l take the following values:

$$\sigma = \begin{Bmatrix} \mathrm{e} \\ \mathrm{o} \end{Bmatrix}, \quad m = 0, 1, 2, \ldots, l, \quad l = 0, 1, \ldots$$

and where the Neumann factor is defined as

$$\varepsilon_m = 2 - \delta_{m0}, \ \textit{i.e.}, \ \begin{cases} \varepsilon_0 = 1 \\ \varepsilon_m = 2, \quad m > 0 \end{cases}$$

The complex vector spherical harmonics, $\boldsymbol{a}_n(\hat{\boldsymbol{r}})$, are[3]

$$\boldsymbol{a}_n(\hat{\boldsymbol{r}}) = \mathrm{i}^{-l+\tau-1}\boldsymbol{A}_n(\hat{\boldsymbol{r}}), \quad \tau = 1, 2 \tag{A.1}$$

In particular,

$$\begin{cases} \boldsymbol{a}_{1\sigma ml}(\hat{\boldsymbol{z}}) = -\delta_{m1}\mathrm{i}^{-l}\sqrt{\dfrac{2l+1}{8\pi}}\hat{\boldsymbol{z}} \times \begin{Bmatrix} \hat{\boldsymbol{x}} \\ \hat{\boldsymbol{y}} \end{Bmatrix} \\ \boldsymbol{a}_{2\sigma ml}(\hat{\boldsymbol{z}}) = \delta_{m1}\mathrm{i}^{-l+1}\sqrt{\dfrac{2l+1}{8\pi}} \begin{Bmatrix} \hat{\boldsymbol{x}} \\ \hat{\boldsymbol{y}} \end{Bmatrix} \end{cases} \tag{A.2}$$

and

$$\begin{cases} \boldsymbol{a}_{1\sigma ml}(-\hat{\boldsymbol{z}}) = -\delta_{m1}\mathrm{i}^{l}\sqrt{\dfrac{2l+1}{8\pi}}\hat{\boldsymbol{z}} \times \begin{Bmatrix} \hat{\boldsymbol{x}} \\ \hat{\boldsymbol{y}} \end{Bmatrix} \\ \boldsymbol{a}_{2\sigma ml}(-\hat{\boldsymbol{z}}) = -\delta_{m1}\mathrm{i}^{l+1}\sqrt{\dfrac{2l+1}{8\pi}} \begin{Bmatrix} \hat{\boldsymbol{x}} \\ \hat{\boldsymbol{y}} \end{Bmatrix} \end{cases} \tag{A.3}$$

The outgoing (or radiating) spherical vector waves $\boldsymbol{u}_{\tau n}(k\boldsymbol{r})$ are

$$\begin{cases} \boldsymbol{u}_{1n}(k\boldsymbol{r}) = \mathrm{h}_l^{(1)}(kr)\boldsymbol{A}_{1n}(\hat{\boldsymbol{r}}) \\ \boldsymbol{u}_{2n}(k\boldsymbol{r}) = \dfrac{(kr\mathrm{h}_l^{(1)}(kr))'}{kr}\boldsymbol{A}_{2n}(\hat{\boldsymbol{r}}) + \sqrt{l(l+1)}\dfrac{\mathrm{h}_l^{(1)}(kr)}{kr}\boldsymbol{A}_{3n}(\hat{\boldsymbol{r}}) \end{cases}$$

and regular spherical vector waves $\boldsymbol{v}_{\tau n}(k\boldsymbol{r})$ as

$$\begin{cases} \boldsymbol{v}_{1n}(k\boldsymbol{r}) = \mathrm{j}_l(kr)\boldsymbol{A}_{1n}(\hat{\boldsymbol{r}}) \\ \boldsymbol{v}_{2n}(k\boldsymbol{r}) = \dfrac{(kr\mathrm{j}_l(kr))'}{kr}\boldsymbol{A}_{2n}(\hat{\boldsymbol{r}}) + \sqrt{l(l+1)}\dfrac{\mathrm{j}_l(kr)}{kr}\boldsymbol{A}_{3n}(\hat{\boldsymbol{r}}) \end{cases}$$

where $\mathrm{j}_l(kr)$ and $\mathrm{h}_l^{(1)}(kr)$ are the spherical Bessel and Hankel functions, respectively.

Appendix B Translation matrices

The translation properties of the vector spherical waves are instrumental for the formulation and the solution of the scattering problem of many individual particles. These translation properties are well know, and we refer to, *e.g.*, [1] for details.

Let $\boldsymbol{r}' = \boldsymbol{r} + \boldsymbol{d}$, see Figure 11. Then

$$\begin{cases} \boldsymbol{v}_n(k\boldsymbol{r}') = \sum\limits_{n'} \mathcal{R}_{nn'}(k\boldsymbol{d})\boldsymbol{v}_{n'}(k\boldsymbol{r}), & \text{for all } \boldsymbol{d} \\ \boldsymbol{u}_n(k\boldsymbol{r}') = \sum\limits_{n'} \mathcal{R}_{nn'}(k\boldsymbol{d})\boldsymbol{u}_{n'}(k\boldsymbol{r}), & r > d \\ \boldsymbol{u}_n(k\boldsymbol{r}') = \sum\limits_{n'} \mathcal{P}_{nn'}(k\boldsymbol{d})\boldsymbol{v}_{n'}(k\boldsymbol{r}), & r < d \end{cases} \tag{B.1}$$

[3]Note the change in definition of $\boldsymbol{a}_n(\hat{\boldsymbol{r}})$ compared to [17] (complex conjugate).

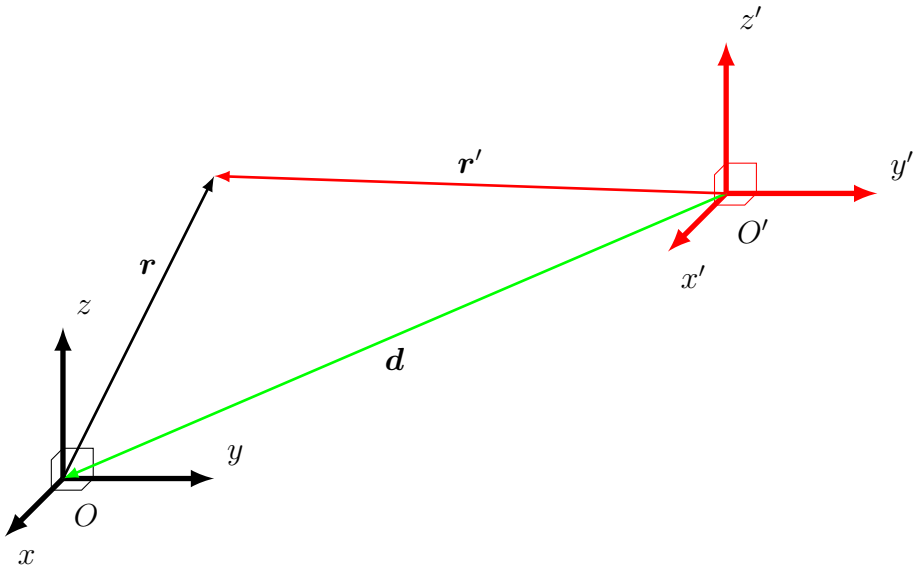

Figure 11: The relation between the translated origins O and O' and the position vectors $\boldsymbol{r}$ and $\boldsymbol{r}'$ at the different origins.

Translation in the opposite direction is identical to the transpose of the translation matrices, *i.e.*,

$$\mathcal{R}^{\mathrm{t}}(k\boldsymbol{d}) = \mathcal{R}(-k\boldsymbol{d}), \quad \mathcal{P}^{\mathrm{t}}(k\boldsymbol{d}) = \mathcal{P}(-k\boldsymbol{d})$$

Denote the spherical coordinates of $\boldsymbol{r}$, $\boldsymbol{r}'$, and $\boldsymbol{d}$ by (r,θ,ϕ), (r',θ',ϕ'), and (d,η,ψ), respectively. The translation matrices for a translation $\boldsymbol{d}$ $(d \le 0)$ are [1]

$$\begin{aligned}
\mathcal{P}_{1\sigma ml,1\sigma m'l'}(k\boldsymbol{d}) &= (-1)^{m'} C_{ml,m'l'}(kd,\eta)\cos(m-m')\psi \\
&\quad + (-1)^{\sigma} C_{ml,-m'l'}(kd,\eta)\cos(m+m')\psi \\
\mathcal{P}_{1\sigma ml,1\sigma' m'l'}(k\boldsymbol{d}) &= (-1)^{m'+\sigma'} C_{ml,m'l'}(kd,\eta)\sin(m-m')\psi \\
&\quad + C_{ml,-m'l'}(kd,\eta)\sin(m+m')\psi, \quad \sigma \neq \sigma' \\
\mathcal{P}_{1\sigma ml,2\sigma' m'l'}(k\boldsymbol{d}) &= (-1)^{m'+\sigma} D_{ml,m'l'}(kd,\eta)\cos(m-m')\psi \\
&\quad - D_{ml,-m'l'}(kd,\eta)\cos(m+m')\psi, \quad \sigma \neq \sigma' \\
\mathcal{P}_{1\sigma ml,2\sigma m'l'}(k\boldsymbol{d}) &= (-1)^{m'} D_{ml,m'l'}(kd,\eta)\sin(m-m')\psi \\
&\quad + (-1)^{\sigma} D_{ml,-m'l'}(kd,\eta)\sin(m+m')\psi \\
\mathcal{P}_{2\sigma ml,\tau\sigma' m'l'}(k\boldsymbol{d}) &= \mathcal{P}_{1\sigma ml,\bar{\tau}\sigma' m'l'}(k\boldsymbol{d}), \quad \tau = 1,2
\end{aligned}$$

where

$$C_{ml,m'l'}(kd,\eta) = \frac{(-1)^{m+m'}}{2}\sqrt{\frac{\varepsilon_m\varepsilon_{m'}}{4}} \times \sum_{\lambda=|l-l'|}^{l+l'} \mathrm{i}^{l'-l+\lambda}(2\lambda+1)\sqrt{\frac{(2l+1)(2l'+1)(\lambda-(m-m'))!}{l(l+1)l'(l'+1)(\lambda+(m-m'))!}} \times \begin{pmatrix} l & l' & \lambda \\ 0 & 0 & 0 \end{pmatrix}\begin{pmatrix} l & l' & \lambda \\ m & -m' & m'-m \end{pmatrix}[l(l+1)+l'(l'+1)-\lambda(\lambda+1)] \times h_\lambda^{(1)}(kd)P_\lambda^{m-m'}(\cos\eta)$$

$$D_{ml,m'l'}(kd,\eta) = \frac{(-1)^{m+m'}}{2}\sqrt{\frac{\varepsilon_m\varepsilon_{m'}}{4}} \times \sum_{\lambda=|l-l'|+1}^{l+l'} \mathrm{i}^{l'-l+\lambda+1}(2\lambda+1)\sqrt{\frac{(2l+1)(2l'+1)(\lambda-(m-m'))!}{l(l+1)l'(l'+1)(\lambda+(m-m'))!}} \times \begin{pmatrix} l & l' & \lambda-1 \\ 0 & 0 & 0 \end{pmatrix}\begin{pmatrix} l & l' & \lambda \\ m & -m' & m'-m \end{pmatrix}\sqrt{\lambda^2-(l-l')^2} \times \sqrt{(l+l'+1)^2-\lambda^2}h_\lambda^{(1)}(kd)P_\lambda^{m-m'}(\cos\eta)$$

where $\varepsilon_m = 2-\delta_{m,0}$ is the Neumann factor, and where $\begin{pmatrix} \cdot & \cdot & \cdot \\ \cdot & \cdot & \cdot \end{pmatrix}$ denotes Wigner's 3j symbol [5], and

$$(-1)^\sigma = \begin{cases} 1, & \sigma = \mathrm{e} \\ -1, & \sigma = \mathrm{o} \end{cases}$$

Note that the factors $\mathrm{i}^{l'-l+\lambda}$ in $C_{ml,m'l'}(d,\eta)$ and $\mathrm{i}^{l'-l+\lambda+1}$ in $D_{ml,m'l'}(d,\eta)$ are always real numbers, due to the conditions on the Wigner's 3j symbol.

The translation matrix $\mathcal{R}_{nn'}(k\boldsymbol{d})$ is identical to $\mathcal{P}_{nn'}(k\boldsymbol{d})$ but with $h_\lambda^{(1)}(kd)$ replaced with $\mathrm{j}_\lambda(kd)$.

We notice that the translation matrices have the form

$$\mathcal{P}_{nn'}(k\boldsymbol{d}) = \sum_{\lambda=|l-l'|+|\tau-\tau'|}^{l+l'} h_\lambda^{(1)}(kd)\left(A_{nn'\lambda}(\psi)P_\lambda^{m-m'}(\cos\eta) + B_{nn'\lambda}(\psi)P_\lambda^{m+m'}(\cos\eta)\right) \tag{B.2}$$

B.1 Average w.r.t. the azimuthal angle

The integral of the translational matrix w.r.t. the azimuthal variable ψ is relevant. Specifically, the quantity $\mathcal{A}_{nn'\lambda} = \int_0^{2\pi} A_{nn'\lambda}(\psi)\,\mathrm{d}\psi + \int_0^{2\pi} B_{nn'\lambda}(\psi)\,\mathrm{d}\psi$ is of inter-

est [15].

$$\mathcal{A}_{nn'\lambda} = \int_0^{2\pi} A_{nn'\lambda}(\phi)\ \mathrm{d}\phi + \int_0^{2\pi} B_{nn'\lambda}(\phi)\ \mathrm{d}\phi$$

$$= 2\pi(-1)^m \delta_{mm'} \begin{array}{c} \\ \text{1e} \\ \text{2o} \\ \text{1o} \\ \text{2e} \end{array} \begin{array}{c} \begin{array}{cccc} \text{1e} & \text{2o} & \text{1o} & \text{2e} \end{array} \\ \begin{pmatrix} C & D & 0 & 0 \\ -D & C & 0 & 0 \\ 0 & 0 & C & -D \\ 0 & 0 & D & C \end{pmatrix} \end{array}, \quad m = 1, 2, \ldots$$

and

$$\mathcal{A}_{nn'\lambda} = \int_0^{2\pi} A_{nn'\lambda}(\phi)\ \mathrm{d}\phi + \int_0^{2\pi} B_{nn'\lambda}(\phi)\ \mathrm{d}\phi$$

$$= 2\pi\delta_{mm'} \begin{array}{c} \\ \text{1e} \\ \text{2o} \\ \text{1o} \\ \text{2e} \end{array} \begin{array}{c} \begin{array}{cccc} \text{1e} & \text{2o} & \text{1o} & \text{2e} \end{array} \\ \begin{pmatrix} C & 0 & 0 & 0 \\ 0 & 0 & 0 & 0 \\ 0 & 0 & 0 & 0 \\ 0 & 0 & 0 & C \end{pmatrix} \end{array}, \quad m = 0$$

where

$$C = C_{mll'\lambda} = \frac{\varepsilon_m}{4} \mathrm{i}^{l'-l+\lambda} (2\lambda+1) \sqrt{\frac{(2l+1)(2l'+1)}{l(l+1)l'(l'+1)}}$$
$$\times \begin{pmatrix} l & l' & \lambda \\ 0 & 0 & 0 \end{pmatrix} \begin{pmatrix} l & l' & \lambda \\ m & -m & 0 \end{pmatrix} [l(l+1) + l'(l'+1) - \lambda(\lambda+1)]$$

$$D = D_{mll'\lambda} = \frac{\varepsilon_m}{4} \mathrm{i}^{l'-l+\lambda+1} (2\lambda+1) \sqrt{\frac{(2l+1)(2l'+1)}{l(l+1)l'(l'+1)}}$$
$$\times \begin{pmatrix} l & l' & \lambda-1 \\ 0 & 0 & 0 \end{pmatrix} \begin{pmatrix} l & l' & \lambda \\ m & -m & 0 \end{pmatrix} \sqrt{\lambda^2 - (l-l')^2} \sqrt{(l+l'+1)^2 - \lambda^2}$$

Appendix C Number density vs. volume fraction

There is a subtle difference between the number density n_0 and the volume fraction f for the slab geometry. To see this, let $V = xyz$ be the volume of a box with sides x, y, and z, and let the number of spheres with radius a inside this box be N. Each sphere has the volume $V_{\text{sphere}} = 4\pi a^3/3$. Then the volume density is

$$f = \frac{NV_{\text{sphere}}}{V} = \frac{NV_{\text{sphere}}}{xyz}$$

On the other hand, the number density counts the number of local origins, N, which lies in a slightly smaller box with sides $x-2a$, $y-2a$, and $z-2a$. The number density n_0 then is

$$n_0 = \frac{N}{(x-2a)(y-2a)(z-2a)} = \frac{fxyz}{V_{\text{sphere}}(x-2a)(y-2a)(z-2a)}$$

Let $x \to \infty$ and $y \to \infty$, keeping the volume fraction f constant, leads to

$$n_0 = \frac{f}{V_{\text{sphere}}(1-2a/z)} = \frac{3f}{4\pi a^3(1-2a/z)}$$

Appendix D Percus-Yevick approximation

The kernel integral $I_l(z)$ in (3.3) determines the kernel entries of the system of integral equations (3.2). This integral is

$$I_l(k;z,a) = k^2 \int_0^\infty g(\sqrt{r_\text{c}^2+z^2})\mathrm{h}_l^{(1)}(k\sqrt{r_\text{c}^2+z^2})\mathrm{P}_l(z/\sqrt{r_\text{c}^2+z^2})r_\text{c}\ \mathrm{d}r_\text{c}, \quad z \in \mathbb{R}$$

For the hole correction (HC) $g(r) = \mathrm{H}(r-2a)$, we have an efficient way of computing this integral [16]. The integral with general pair correlation function $g(r)$ is most conveniently solved by adding and subtracting the HC. The remaining integral to calculate then is

$$I_l^{\text{Corr}}(k;z,a) = k^2 \int_{h(z)}^\infty \Big(g(\sqrt{r_\text{c}^2+z^2})-1\Big)\,\mathrm{h}_l^{(1)}(k\sqrt{r_\text{c}^2+z^2})\mathrm{P}_l(z/\sqrt{r_\text{c}^2+z^2})r_\text{c}\ \mathrm{d}r_\text{c}$$

where

$$h(z) = \begin{cases} \sqrt{4a^2-z^2}, & -2a \le z \le 2a \\ 0, & |z| > 2a \end{cases}$$

D.1 Hard spheres

For hard spheres in a particulate material without boundaries, the Percus-Yevick (P-Y) approximation [21] can be evaluated exactly. We follow [25, 28] closely, and start by defining the function

$$h(\boldsymbol{r}) = g(\boldsymbol{r}) - 1, \quad \boldsymbol{r} \in \mathbb{R}^3$$

This function satisfies the Ornstein-Zernike equation

$$h(\boldsymbol{r}) = c(\boldsymbol{r}) + n_0 \iiint_{\mathbb{R}^3} c(\boldsymbol{r}')h(\boldsymbol{r}-\boldsymbol{r}')\,\mathrm{d}v', \quad \boldsymbol{r} \in \mathbb{R}^3$$

where $c(\boldsymbol{r})$ is the direct correlation function. The integral defines the indirect correlation function $h(\boldsymbol{r})$. Ornstein-Zernike equation is of convolution type, and its Fourier transform is

$$\hat{h}(\boldsymbol{\xi}) = \hat{c}(\boldsymbol{\xi}) + n_0\hat{c}(\boldsymbol{\xi})\hat{h}(\boldsymbol{\xi}), \quad \boldsymbol{\xi} \in \mathbb{R}^3$$

with solution

$$\hat{h}(\boldsymbol{\xi}) = \frac{\hat{c}(\boldsymbol{\xi})}{1 - n_0\hat{c}(\boldsymbol{\xi})}, \quad \boldsymbol{\xi} \in \mathbb{R}^3$$

The structure factor $S(\boldsymbol{\xi})$ is defined as

$$S(\boldsymbol{\xi}) = 1 + n_0\hat{h}(\boldsymbol{\xi})$$

The direct correlation function $c(\boldsymbol{r})$ is now determined. It is convenient to introduce a new function $y(\boldsymbol{r})$ as ($R = 2a$)

$$y(\boldsymbol{r}) = \begin{cases} -c(\boldsymbol{r}), & r < R \\ g(\boldsymbol{r}), & r \geq R \end{cases}$$

D.2 The Percus-Yevick approximation

In the P-Y approximation, we replace $h(\boldsymbol{r}) - c(\boldsymbol{r})$ with $y(\boldsymbol{r}) - 1$ everywhere in space. We then have

$$c(\boldsymbol{r}) = \begin{cases} -y(\boldsymbol{r}), & r < R \\ h(\boldsymbol{r}) + 1 - g(\boldsymbol{r}) = 0, & r \geq R \end{cases}$$

and the Ornstein-Zernike equation becomes

$$y(\boldsymbol{r}) - 1 = -n_0 \iiint\limits_{r'<R} y(\boldsymbol{r}')(g(\boldsymbol{r} - \boldsymbol{r}') - 1)\,\mathrm{d}v', \quad \boldsymbol{r} \in \mathbb{R}^3$$

or

$$y(\boldsymbol{r}) = 1 + n_0 \iiint\limits_{\substack{r'<R \\ |\boldsymbol{r}-\boldsymbol{r}'|<R}} y(\boldsymbol{r}')\ \mathrm{d}v' - n_0 \iiint\limits_{\substack{r'<R \\ |\boldsymbol{r}-\boldsymbol{r}'|\geq R}} y(\boldsymbol{r}')(y(\boldsymbol{r} - \boldsymbol{r}') - 1)\ \mathrm{d}v'$$

This has a closed form solution for $c(\boldsymbol{r})$, $r < R$ can be obtained [28]

$$c(\boldsymbol{r}) = c(r) = \begin{cases} \alpha + \beta(r/R) + \delta(r/R)^3, & r < R \\ 0, & r \geq R \end{cases}$$

where

$$\begin{cases} \alpha = -\dfrac{(1+2f)^2}{(1-f)^4} \\ \beta = 6f\dfrac{(1+f/2)^2}{(1-f)^4} \end{cases} \qquad \begin{cases} \delta = -f\dfrac{(1+2f)^2}{2(1-f)^4} \\ f = \dfrac{n_0\pi R^3}{6} \end{cases}$$

with Fourier transform

$$\hat{c}(\boldsymbol{\xi}) = \hat{c}(\xi) = \iiint\limits_{\mathbb{R}^3} c(r)\mathrm{e}^{-\mathrm{i}\boldsymbol{\xi}\cdot\boldsymbol{r}}\,\mathrm{d}v = 4\pi\int_0^R \left(\alpha + \beta(r/R) + \delta(r/R)^3\right)\mathrm{j}_0(\xi r)\,r^2\,\mathrm{d}r$$

$$= \frac{4\pi R^3}{\xi R}\int_0^1 \left(\alpha x + \beta x^2 + \delta x^4\right)\sin(\xi R x)\ \mathrm{d}x = 4\pi R^3 F(\xi R)$$

where we introduced the function $F(x)$, defined as

$$F(x) = A(x) + B(x)\sin(x) + C(x)\cos(x) = O(1/x^2), \quad \text{as } x \to \infty \tag{D.1}$$

where

$$\begin{cases} A(x) = \dfrac{24\delta}{x^6} - \dfrac{2\beta}{x^4} \\ B(x) = \dfrac{\alpha + 2\beta + 4\delta}{x^3} - \dfrac{24\delta}{x^5} \\ C(x) = -\dfrac{\alpha + \beta + \delta}{x^2} + \dfrac{2\beta + 12\delta}{x^4} - \dfrac{24\delta}{x^6} \end{cases}$$

Finally,

$$h(\boldsymbol{r}) = h(r) = \frac{1}{8\pi^3} \iiint\limits_{\mathbb{R}^3} \frac{\hat{c}(\boldsymbol{\xi})}{1 - n_0\hat{c}(\boldsymbol{\xi})} \mathrm{e}^{\mathrm{i}\boldsymbol{\xi}\cdot\boldsymbol{r}} \, \mathrm{d}\xi^3 = \frac{1}{2\pi^2 r} \int_0^\infty \frac{\hat{c}(\xi)}{1 - n_0\hat{c}(\xi)} \sin(\xi r)\, \xi \, \mathrm{d}\xi$$

Reformulate the solution to

$$h(r) = \frac{2R}{\pi r} \int_0^\infty \frac{xF(x)}{1 - 24fF(x)} \sin(xr/R) \, \mathrm{d}x$$

and $g(r) = h(r) + 1$.

The integral in the computation of the function $h(r)$ is poorly converging at infinity, and we need to extract the slowly converging tail. Make an asymptotic analysis of the integrand as $x \to \infty$. We get

$$\frac{xF(x)}{1 - 24fF(x)} = G(x) + O(x^{-3})$$

where

$$G(x) = (\alpha + 2\beta + 4\delta)\frac{\sin(x)}{x^2} - (\alpha + \beta + \delta)\frac{\cos(x)}{x} \tag{D.2}$$

Use the integrals [11]

$$\int_0^\infty \frac{\cos(x)\sin(\eta x)}{x} \, \mathrm{d}x = \frac{\pi}{2}, \quad \eta > 1$$

and

$$\int_0^\infty \frac{\sin(x)\sin(\eta x)}{x^2} \, \mathrm{d}x = \frac{\pi}{2}, \quad \eta > 1$$

to evaluate ($\eta = r/R \in [1, \infty)$)

$$h(r) = 9f\frac{1+f}{2\eta(1-f)^3} + \frac{2}{\eta\pi} \int_0^\infty \left(\frac{xF(x)}{1 - 24fF(x)} - G(x) \right) \sin(\eta x) \, \mathrm{d}x$$

References

[1] A. Boström, G. Kristensson, and S. Ström. Transformation properties of plane, spherical and cylindrical scalar and vector wave functions. In V. V. Varadan, A. Lakhtakia, and V. K. Varadan, editors, *Field Representations and Introduction to Scattering*, Acoustic, Electromagnetic and Elastic Wave Scattering, chapter 4, pages 165–210. Elsevier Science Publishers, Amsterdam, 1991.

[2] P. Bouguer. *Essai d'optique sur la gradation de la lumière*. Claude Jombert, Paris, 1729.

[3] V. N. Bringi, V. K. Varadan, and V. V. Varadan. Average dielectric properties of discrete random media using multiple scattering theory. *IEEE Trans. Antennas Propag.*, **31**(2), 371–375, 1983.

[4] V. N. Bringi, V. V. Varadan, and V. K. Varadan. The effects on pair correlation function of coherent wave attenuation in discrete random media. *IEEE Trans. Antennas Propag.*, **30**(4), 805–808, 1982.

[5] A. R. Edmonds. *Angular Momentum in Quantum Mechanics*. Princeton University Press, Princeton, NJ, 3 edition, 1974.

[6] J. Fikioris and P. Waterman. Multiple scattering of waves. III. The electromagnetic case. *J. Quant. Spectrosc. Radiat. Transfer*, **123**, 8–16, 2013.

[7] L. L. Foldy. The multiple scattering of waves. I. general theory of isotropic scattering by randomly distributed scatterers. *Phys. Rev.*, **67**, 107–119, Feb 1945.

[8] A. L. Gower and G. Kristensson. Effective waves for random three-dimensional particulate materials. *New Journal of Physics*, **23**(6), 063083, 2021.

[9] A. L. Gower, I. D. Abrahams, and W. J. Parnell. A proof that multiple waves propagate in ensemble-averaged particulate materials. *Proc. R. Soc. A*, **475**(2229), 20190344, 2019.

[10] A. L. Gower, W. J. Parnell, and I. D. Abrahams. Multiple waves propagate in random particulate materials. *SIAM J. Appl. Math.*, **79**(6), 2569–2592, 2019.

[11] I. S. Gradshteyn and I. M. Ryzhik. *Table of Integrals, Series, and Products*. Academic Press, San Diego, CA, seventh edition, 2007.

[12] M. Gustavsson, G. Kristensson, and N. Wellander. Multiple scattering by a collection of randomly located obstacles. Part II: Numerical implementation — coherent fields. Technical Report LUTEDX/(TEAT-7236)/1–15/(2014), Lund University, Department of Electrical and Information Technology, P.O. Box 118, S-221 00 Lund, Sweden, 2014.

[13] A. Ishimaru. *Wave Propagation and Scattering in Random Media*. IEEE Press, New York, 1997.

[14] R. Kress. *Linear Integral Equations*. Springer-Verlag, Berlin Heidelberg, second edition, 1999.

[15] G. Kristensson. Coherent scattering by a collection of randomly located obstacles — an alternative integral equation formulation. *J. Quant. Spectrosc. Radiat. Transfer*, **164**, 97–108, 2015.

[16] G. Kristensson. Evaluation of some integrals relevant to multiple scattering by randomly distributed obstacles. *Journal of Mathematical Analysis and Applications*, **432**(1), 324–337, 2015.

[17] G. Kristensson. *Scattering of Electromagnetic Waves by Obstacles*. Mario Boella Series on Electromagnetism in Information and Communication. SciTech Publishing, Edison, NJ, USA, 2016.

[18] M. Lax. Multiple scattering of waves. II. The effective field in dense systems. *Phys. Rev.*, **85**, 621–629, Feb 1952.

[19] M. I. Mishchenko. *Electromagnetic Scattering by Particles and Particle Groups. An Introduction*. Cambridge University Press, New York, NY, 2014.

[20] R. K. Pathria and P. D. Beale. *Statistical Mechanics*. Elsevier/Academic Press, fourth edition, 2022.

[21] J. K. Percus and G. J. Yevick. Analysis of classical statistical mechanics by means of collective coordinates. *Phys. Rev.*, **110**(1), 1, 1958.

[22] V. P. Tishkovets, E. V. Petrova, and M. I. Mishchenko. Scattering of electromagnetic waves by ensembles of particles and discrete random media. *J. Quant. Spectrosc. Radiat. Transfer*, **112**, 2095–2127, 2011.

[23] L. Tsang, J. Kong, and T. Habashy. Multiple scattering of acoustic waves by random distribution of discrete spherical scatterers with the quasicrystalline and Percus–Yevick approximation. *J. Acoust. Soc. Am.*, **71**(3), 552–558, 1982.

[24] L. Tsang and J. A. Kong. *Scattering of Electromagnetic Waves: Advanced Topics*. John Wiley & Sons, New York, NY, 2001.

[25] L. Tsang, J. A. Kong, K.-H. Ding, and C. O. Ao. *Scattering of Electromagnetic Waves: Numerical Simulations*. John Wiley & Sons, New York, NY, 2001.

[26] V. K. Varadan, V. N. Bringi, and V. V. Varadan. Coherent electromagnetic wave propagation through randomly distributed dielectric scatterers. *Phys. Rev. D*, **19**(8), 2480–2489, April 1979.

[27] V. K. Varadan, V. N. Bringi, V. V. Varadan, and A. Ishimaru. Multiple scattering theory for waves in discrete random media and comparison with experiments. *Radio Sci.*, **18**(3), 321–327, 1983.

[28] M. S. Wertheim. Exact solution of the Percus-Yevick integral equation for hard spheres. *Phys. Rev. Lett.*, **10**(8), 321–323, 1963.